NANO · MICRO small
www.small-journal.com

Doping-Induced Surface and Grain Boundary Effects in Ni-Rich Layered Cathode Materials

*Liang-Yin Kuo, Christoph Roitzheim, Helen Valencia, Joachim Mayer, Sören Möller, Seung-Taek Myung, Martin Finsterbusch, Olivier Guillon, Dina Fattakhova-Rohlfing, and Payam Kaghazchi**

In this work, the effects of dopant size and oxidation state on the structure and electrochemical performance of $LiNi_{0.8}Co_{0.1}Mn_{0.1}O_2$ (NCM811) are investigated. It is shown that doping with boron (B) which has a small ionic radius and an oxidation state of 3+, leads to the formation of a boron oxide-containing surface coating (probably Li_3BO_3), mainly on the outer surface of the secondary particles. Due to this effect, boron only slightly affects the size of the primary particle and the initial capacity, but significantly improves the capacity retention. On the other hand, the dopant ruthenium (Ru) with a larger ionic radius and a higher oxidation state of 5+ can be stabilized within the secondary particles and does not experience a segregation to the outer agglomerate surface. However, the Ru dopant preferentially occupies incoherent grain boundary sites, resulting in smaller primary particle size and initial capacity than for the B-doped and pristine NCM811. This work demonstrates that a small percentage of dopant (2 mol%) cannot significantly affect bulk properties, but it can strongly influence the surface and/or grain boundary properties of microstructure and thus the overall performance of cathode materials.

1. Introduction

Li-ion batteries (LIBs) are becoming increasingly important due to the growing demand for portable electronic devices and electric vehicles (EVs).[1] In particular, the development of high energy density LIBs for EVs, is an important issue due to the increasing environmental concerns. Many efforts have been made to find novel cathode materials to replace $LiCoO_2$ (LCO), which dominated the first generation of commercial LIBs, by alternative layered oxides containing less toxic and expensive elements.[2] In addition, a novel cathode material should provide reasonably high energy density and safety, as well as, long cycle life. Ni-rich NCM materials such as $LiNi_{0.8}Co_{0.1}Mn_{0.1}O_2$ (NCM811)[3] are currently among the most promising cathodes that can meet the aforementioned requirements. Although they can provide a better electrochemical

L.-Y. Kuo
Department of Chemical Engineering
Ming Chi University of Technology
No. 84, Gongzhuan Rd., New Taipei City 243303, Taiwan

C. Roitzheim, S. Möller, M. Finsterbusch, O. Guillon, D. Fattakhova-Rohlfing, P. Kaghazchi
Institute of Energy and Climate Research
Materials Synthesis and Processing (IEK-1)
Forschungszentrum Jülich GmbH
52425 Jülich, Germany
E-mail: p.kaghazchi@fz-juelich.de

H. Valencia, J. Mayer
Central Facility for Electron Microscopy (GFE)
RWTH Aachen University
52074 Aachen, Germany

The ORCID identification number(s) for the author(s) of this article can be found under https://doi.org/10.1002/smll.202307678

DOI: 10.1002/smll.202307678

H. Valencia, J. Mayer
Ernst Ruska-Centre (ER-C 2)
Forschungszentrum Jülich GmbH
52425 Jülich, Germany

S.-T. Myung
Department of Nanotechnology and Advanced Materials Engineering
Sejong University
98 Gunja-dong, Gwangjin-gu, Seoul 05006, South Korea

D. Fattakhova-Rohlfing
Faculty of Engineering and Center for Nanointegration Duisburg-Essen
CENIDE
University Duisburg-Essen
Lotharstraße 1, 47057 Duisburg, Germany

P. Kaghazchi
MESA+ Institute for Nanotechnology
University of Twente
P. O. Box 217, Enschede 7500AE, The Netherlands

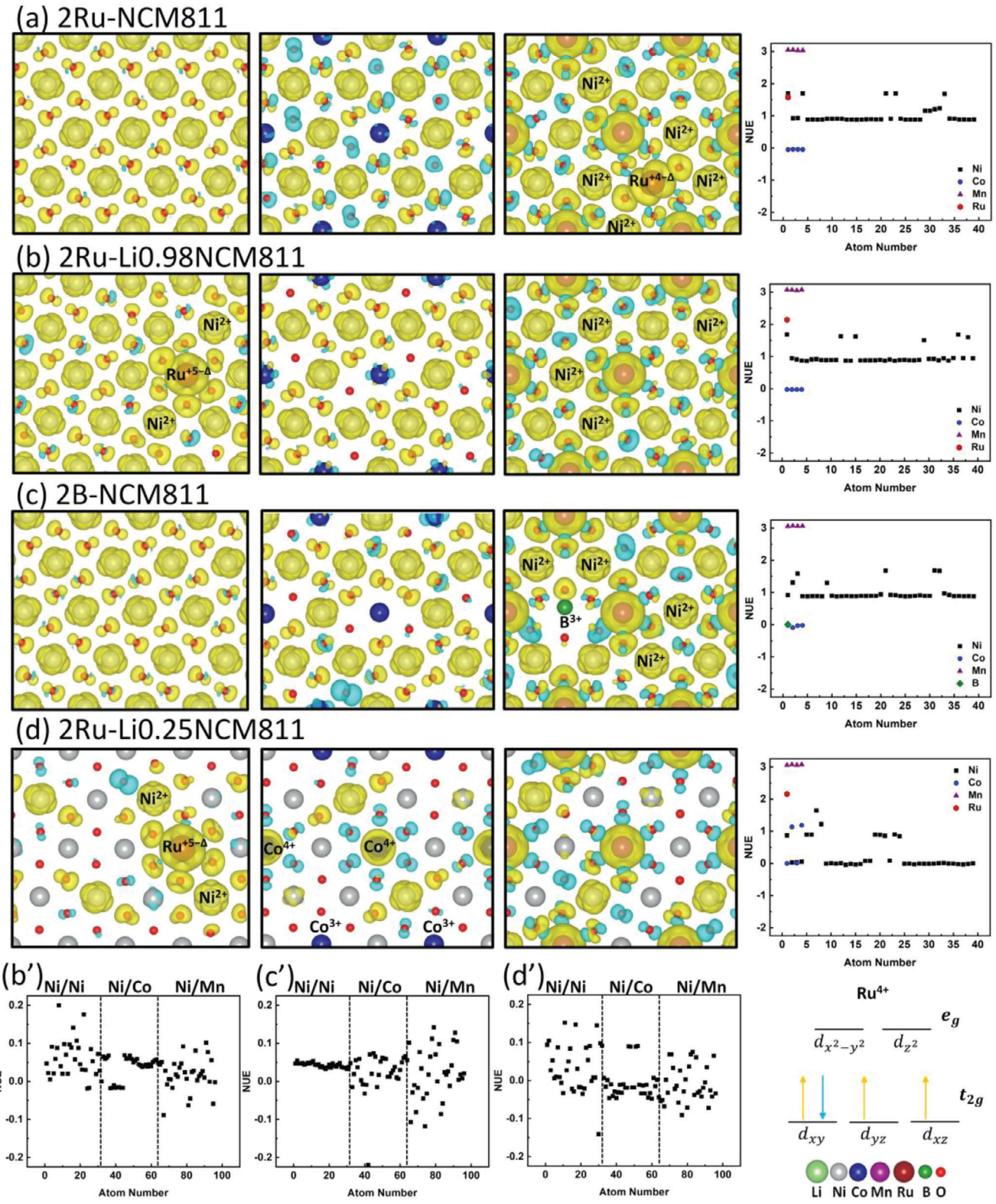

Figure 1. Computed spatial spin density difference (SDD) and number of unpaired electrons (NUE) on Ni, Co, Mn, Ru, and B for a) 2Ru-NCM811 (Model I), b) 2Ru-Li0.98NCM811 (Model II) c) 2B-NCM811, and d) 2Ru-Li0.25NCM811 (Model II). The yellow and blue features in SDD plots represent up- and down-spin electrons. A SDD isosurface of 0.007 was used for all structures.

Table 1. Computed lattice parameters of NCM811, Ru-doped NCM811 in model (I) and (II), and B-doped NCM811 and their corresponding experimental results. The experimental results for NCM811 and 2B-NCM811 are reprinted with permission from ref. [7a] Copyright 2022, American Chemical Society.

	Theory			Experiment		
	a [Å]	*b* [Å]	*c* [Å]	*a* [Å]	*b* [Å]	*c* [Å]
NCM811	2.889	2.879	14.301	2.870(4)	–	14.196(4)
2Ru-NCM811 (model I)	2.915	2.874	14.298	2.876(4)	–	14.208(5)
2Ru-Li0.98NCM811 (model II)	2.915	2.895	14.366	–	–	–
2B-NCM811	2.917	2.862	14.339	2.874(4)	–	14.206(4)

performance compared to LCO, they still suffer from poor thermal stability and severe capacity fading during long-term cycling.[4] Doping and coating are promising strategies to improve the capacity retention of NCM cathodes.[5] Numerous ions such as Mg^{2+},[6] B^{3+},[7] Al^{3+},[7b,8] Ga^{3+},[9] Fe^{3+},[10] Sb^{3+},[4a] Zr^{4+},[11] Ru^{4+},[12] Nb^{5+},[13] W^{6+},[14] and Mo^{6+},[15] have already been investigated as the dopants for the NCM structure. The size and oxidation state of the dopants are expected to critically affect the properties of the host materials. Therefore, understanding their effects on the crystalline structure and morphology of NCM host materials is very important for the rational development of efficient NCM cathodes. Boron (B^{3+}) and ruthenium (Ru^{4+}) are particularly interesting ions to study the effects of dopants due to their different size and oxidation state. Boron is a light element and has the smallest ionic radius compared to other commonly studied dopants (0.27 Å for B^{3+} compared to 0.68 Å for Ru^{3+}).[16] Ruthenium can have a high oxidation state (up to 5+) compared to Ni (up to 4+). In $Na[Ni_{2/3}Ru_{1/3}]O_2$, which is used as a cathode material for sodium-ion batteries, Ru has the oxidation state 5+, and due to its higher Pauling electronegativity of 2.2 compared to Ni (1.91), the Ru—O bond is likely to be partially covalent. The more pronounced covalent character of the transition metal (TM) with oxygen stabilizes the oxygen redox reaction, mitigates the release of oxygen gas, and increases the structural rigidity.[16–17] Ru doping also drastically improved the rate performance of spinel $LiNi_{0.5}Mn_{1.5}O_4$.[18] Little has been reported on Ru as a dopant in NCM cathodes for LIBs. As far as the authors are aware, only Song et al.[19] investigated the effect of Ru doping on the structure and electrochemical properties of a Li-rich system, namely $Li(Li_{0.20}Mn_{0.54}Ni_{0.13}Co_{0.13})O_2$, and reported an increase in interlayer spacing, enhanced Li diffusion, and improved capacity retention during cycling. The superior performance of B-doped NCM cathodes has already been investigated in several publications.[7a,20] A multiscale modeling simulation (a combination of density functional theory (DFT), ab initio atomistic thermodynamics, and continuum mechanics) from our group has found for the first time the reason for the enhanced the stability of B-doped Ni-rich cathodes.[20c] It was

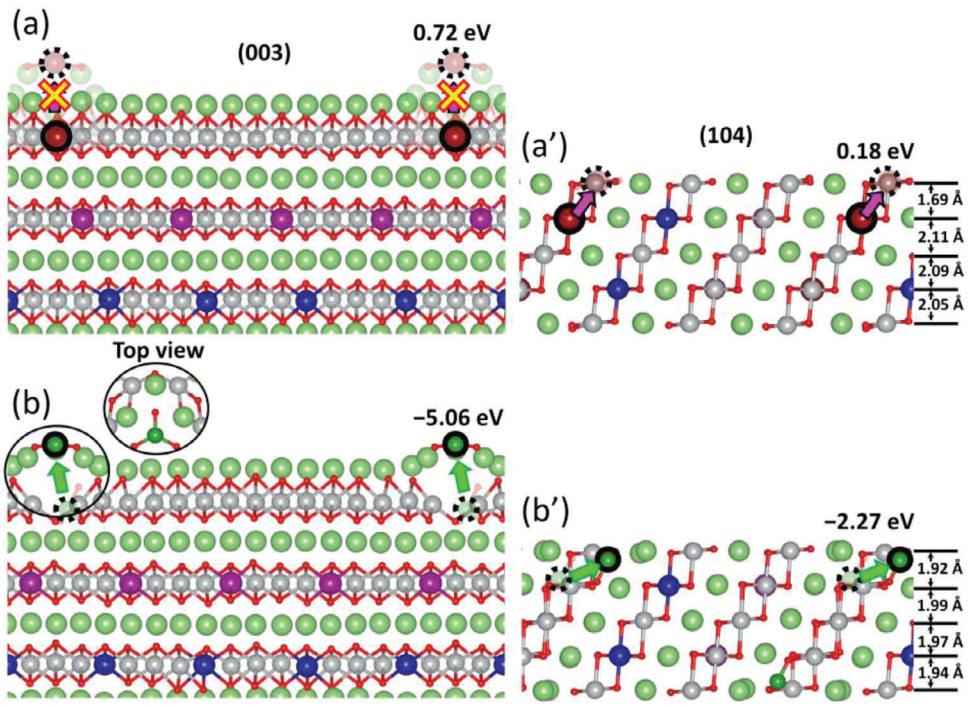

Figure 2. Side views of a) 2Ru-Li0.98NCM811 and b) 2B-NCM811 on (003) and (104) surfaces and their interlayer separation distance on (104) surfaces. The inset shows the top view of BO_3 triangles.

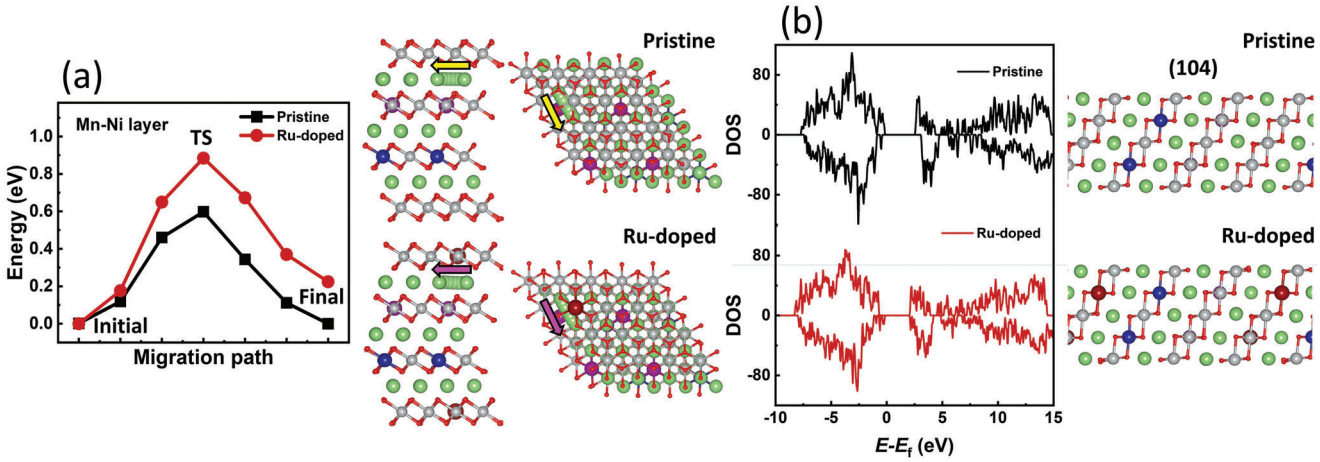

Figure 3. a) Diffusion mechanisms of pristine and Ru-doped NCM811 b) Density of states (DOS) of (104) surface for pristine (black), and Ru-doped NCM811 (red).

shown that B doping leads to the formation of a Li_3BO_3 layer on the (001) surfaces of $LiNiO_2$[20c] and $LiNi_{0.92}Co_{0.04}Al_{0.04}O$.[21] This leads to an increase in the chemical stability of the above mentioned cathode interfaces with the electrolyte as well as a change in the microstructure morphology, resulting in higher integrity. This result has been confirmed by electrochemical tests of Ni-rich NCM and NCA cathodes, which showed a better capacity retention compared to the bare systems.[20c] However, to our knowledge, the effects of dopant size and oxidation on the properties of NCM811 have not been investigated so far. To fill this knowledge gap, we have performed in detail theoretical and experimental investigation of Ru-doped $LiNi_{0.8}Co_{0.1}Mn_{0.1}O_2$ (Ru-NCM811) and completed our recent studies on B-doped $LiNi_{0.8}Co_{0.1}Mn_{0.1}O_2$ (B-NCM811) to compare the impact of Ru and B on bulk, surface, grain boundaries, and microstructures of NCM811.

2. Results and Discussion

2.1. Theory

Our extensive electrostatic analysis and DFT calculations with Perdew–Burke–Ernzerhof (PBE) functional, PBE with Hubbard U (PBE+U), and Heyd–Scuseria–Ernzerhof (HSE) functionals show that the preferred occupation site and oxidation state of Ru correlates with the mechanism of charge balance. To find

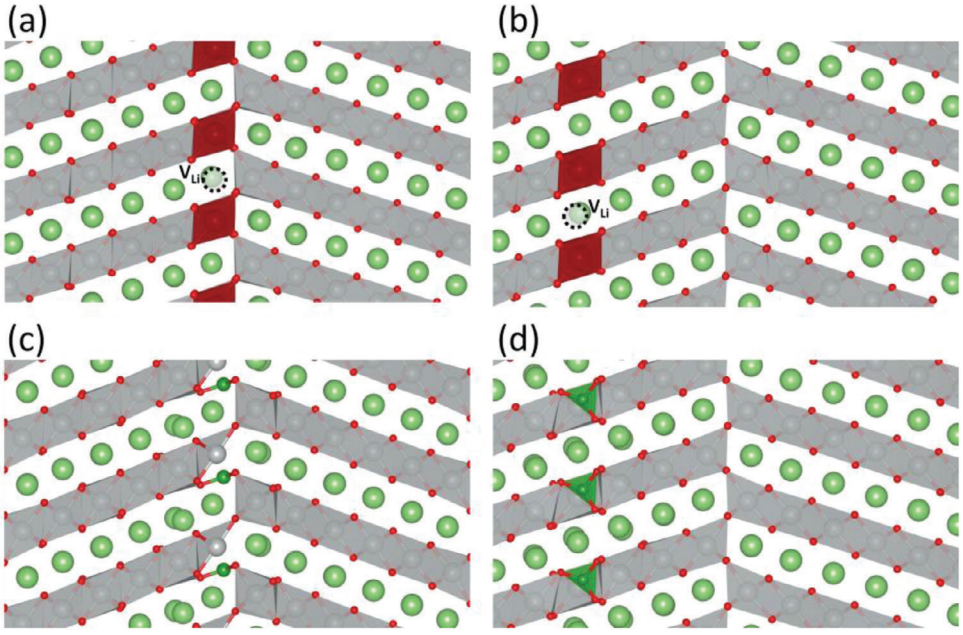

Figure 4. Atomistic structure of the coherent twin grain boundary GB $\Sigma3[110]/(1\bar{1}2)$ of $LiNiO_2$ with Ru and V_{Li} at a) GB and in b) bulk as well as B at c) GB and in d) bulk.

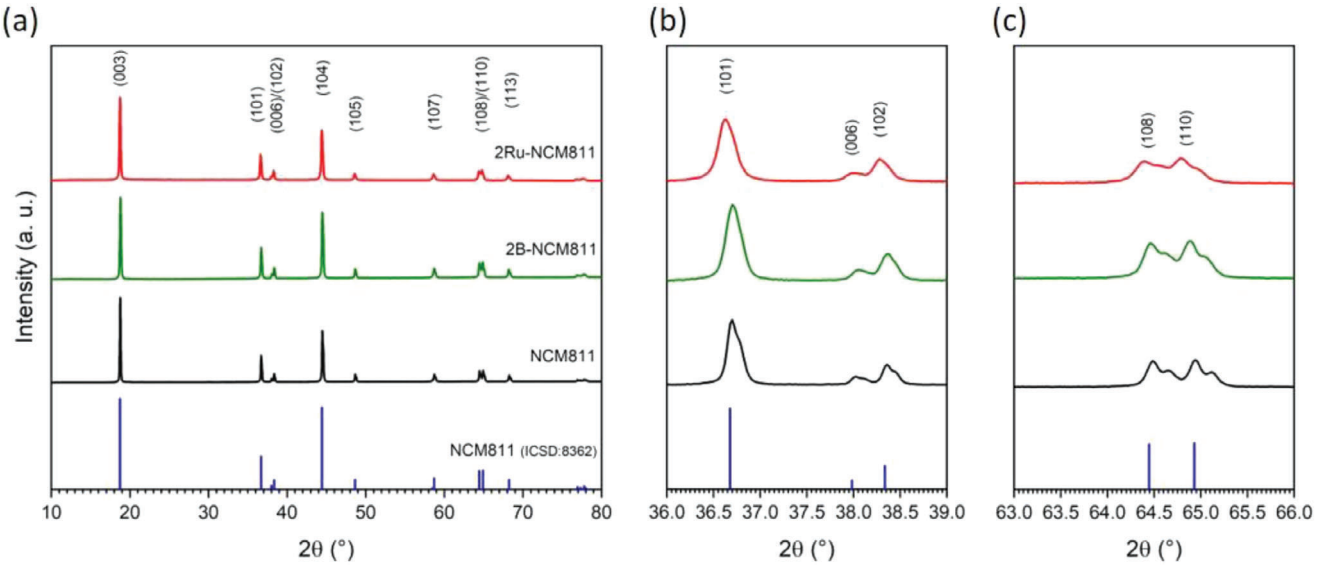

Figure 5. a) Powder XRD patterns of pristine NCM811, 2B-NCM811, and 2Ru-NCM811. b,c) Magnifications of selected 2θ-regions from a). The patterns for NCM811 and 2B-NCM811 are reprinted with permission from ref. [7a]. Copyright 2022, American Chemical Society.

the realistic model, we studied two structures that can lead to different charge balancing mechanisms (see **Figure 1**), namely: I) 1Ru → 1Ni (2Ru-NCM811) and II) 1Ru → 1Ni + $1V_{Li}$ (2Ru-Li0.98NCM811). The number of unpaired electrons (NUE) on ions and spin density difference (SDD) are illustrated in Figure 1. The DFT-HSE calculation shows that to compensate the $4Mn^{4+}$ → $4Ni^{3+}$ replacement in pristine and doped NCM811(modeled by LixNi) systems the following reduction takes place: $4Ni^{3+}$ → $4Ni^{2+}$, which can be seen in Figure S1a–d (Supporting Information) (NUE > 1.55 for Ni^{2+} and NUE < 1.55 for Ni^{3+}). Any additional reduced Ni cations, besides $4Ni^{2+}$, should be due to the Ru → Ni doping. For the model I, namely 1Ru → 1Ni (2Ru-NCM811), Ru prefers to occupy a Ni site close to Mn cations. The SDD plot (Figure 1a) shows a small oxidation of several O anions close to Ru and Ni cations, indicating a delocalization of electrons between Ru and O as well as Ni and O (probably due to the overlap between Ru_{4d}, $Ni_{3d,}$ and O_{2p} orbitals). Based on the shape of SDD feature and the NUE value of > 1 for Ru, we propose the formation of $Ru^{+4-\Delta} - O^{-2+\Delta}$ and $Ni^{+3-\Delta'} - O^{-2+\Delta'}$ (Figure 1a). This means that to compensate the formation of $1Ru^{+4-\Delta}$, 1Ni cation is reduced (Figure 1a: $4Ni^{2+}$ for $4Mn^{4+}$ and $1Ni^{2+}$ for $1Ru^{+4-\Delta}$ in the supercell). For the model II, namely 1Ru → 1Ni + $1V_{Li}$ (2Ru-Li0.98NCM811), Ru prefers to occupy a Ni site in the TM layer where only Ni (and no Co or Mn) is present (Figure 1b). Several nearest neighbor O anions of Ru and 2Ni cations experience a small oxidation. From the shape of SDD and the NUE value larger than 2 for Ru (see Figure 1b'), we propose the formation of $Ru^{+5-\Delta} - O^{-2+\Delta}$ and $Ni^{+3-\Delta'} - O^{-2+\Delta'}$. Thus, the large charge state of $1Ru^{+5-\Delta}$ is compensated by $2Ni^{+3-\Delta'}$+$1V_{Li}$. An enhanced Ni^{2+} amount was also observed based on X-ray diffraction (XRD) for the Ru-doped sample (Table S2, Supporting Information), which will be discussed later in this article. In comparison to model I (Ru → Ni with Ru at the Ni/Mn layer), the estimated charge state of Ru as well as the Ru-doping induced change in lattice parameters (Δa and Δc) for model II (Ru → Ni + $1V_{Li}$ with Ru at the Ni layer) is in better agreement with our X-ray photoelectron spectroscopy (XPS) and XRD data (Figure 6 and **Table 1**). We have recently studied the B-doped NCM811 system.[7a] B was found to occupy a tetrahedral site and since it has a charge state of 3+ (similar to the replaced Ni^{3+}), no significant change in the oxidation state of other Ni cations is expected after B doping as the formation of $4Ni^{2+}$ cations is because of the presence of $4Mn^{4+}$ (see Figure 1c).

The DFT-calculated lattice parameters a and c for NCM811, 2Ru-Li0.98NCM811 (model II), and 2B-NCM811 are in qualitative agreement with our XRD data (Table 1). As the computed doping-induced increase in a and c is larger than the corresponding experimental values, we conclude that in fact only a small amount of dopants can be found in the bulk lattice, and the rest are present on the surface and/or grain boundaries (GBs) as will be discussed later in this manuscript.

The influence of Ru- and B-doping on the lithiation/delithiation-induced change in a ($|\Delta a|$) and c ($|\Delta c|$) was also computed (Figure S2, Supporting Information) to be small: $|\Delta a| \leq 0.14\%$ and $|\Delta c| \leq 0.06\%$. Our in-situ XRD data confirm that $|\Delta a|$ and $|\Delta c|$ are small for the Ru-doped case (Figure S3, Supporting Information). A previous experimental study also showed that B doping has a minor effect on the lattice parameters change during cycling ($|\Delta a| = 0.20\%$ and $|\Delta c| = 5.9\%$ for pristine NCM90 versus $|\Delta a| = 0.19\%$ and $|\Delta c| = 5.1\%$ for 1 mol% B-doped NCM90).[20c] As the impact of doping on $|\Delta a|$ and $|\Delta c|$ is slightly overestimated in our calculation (Figure S2, Supporting Information) compared to experiment (Figures S3 and S5b in ref. [20c], Supporting Information) we again conclude that the concentration of lattice doping in the real system should be smaller than that in our modeled structure (2% Ru or B), and a large portion of dopant content should be either at surfaces or grain boundaries of NCM811 particles. This result also indicates that the integrity of NCM811 secondary particles (i.e., cycling performance) cannot be affected by Ru or B bulk lattice doping, as the delithiation/lithiation-induced Δa

and Δc cannot be suppressed by a small amount of dopants in the bulk. However, the presence of dopants at the surface of agglomerate (in the B-doped case) and/or at grain boundaries (in the Ru-doped case) can strongly influence the capacity and cycling stability of NCM811, which will be discussed later in this article.

To understand the effect of Ru doping on delithiation-induced oxidation mechanism in NCM811, we computed NUE and SDD for 2Ru-NCM811 (model II) with a 0.25 Li concentration (Figure 1d). It is found that the computed NUE of 77% Ni cations decrease, which can also be seen by their small and disappeared SDD features, compared to those of Ni ones at the high Li concentration case (Figure 1b). This indicates the oxidation of 3% $Ni^{2+} \rightarrow Ni^{3+}$ and 64% $Ni^{3+} \rightarrow Ni^{4+}$ and 10% $Ni^{2+} \rightarrow Ni^{4+}$ for 2Ru-Li0.98NCM811 → 2Ru-Li0.25NCM811. However, the oxidation state of 2 Ni (5%) close to Ru cations at the Ni/Ni layer remains 2+. The computed NUE and the SDD features on Ru remain the same but the oxidation of O increases in the Ni/Ni layer (Figure 1d'). Moreover, half of Co shows the increase in the computed NUE and SDD features indicating 50% $Co^{3+} \rightarrow Co^{4+}$ oxidation. The oxidation state of Mn remains 4+ with unchanged NUE and SDD features.

To study the tendency of Ni, Ru, and B to segregate to the surface of NCM811, we focused on two probable orientations in layered oxide materials, namely (003) and (104), which have been observed experimentally and predicted by simulation on $LiNiO_2$[20c] and $LiNi_{0.92}Co_{0.04}Al_{0.04}O_2$.[21] Our calculation indicates that Ni prefers to segregate to the topmost surface layers, while the Co and Mn are homogeneously distributed in the bulk region. In our previous work on $LiNiO_2$(003),[20c] we found that boron, which was at the subsurface Ni site in the initial structure, moves to the topmost layer after geometry relaxation. Simultaneously, the B dopant dragged three O anions to the surface and rearranged several surface Li ions forming a Li_3BO_3-like structure. In this work, we computed how much is the energy gain for this process on Ru- and B-doped NCM811(003) surface. It is found that Ru prefers binding to the Ni subsurface sites, and probably in the bulk region, on (003) as well as (104) surfaces. The segregation energy (the energy difference between structures with dopant in the subsurface and surface sites: $\Delta E_S = E_{surf} - E_{subs}$) of Ru for the (003) and (104) surfaces is 0.72 eV per atom and 0.18 eV per atom, respectively (**Figure 2a**). The computed ΔE_S value for B doping is, however, −5.06 and −2.27 eV, respectively, for the (003) and (104) surfaces. This clearly shows that B tends to migrate to the surface of both cases (Figure 2b). As the average B– O bond lengths in the formed BO_3 triangles (≈1.39 Å) at the topmost layer of (003) surface (insert in Figure 2b) is very similar to that of α-Li_3BO_3 (monoclinic P2x/c) reported by Stewner,[22] the B-doping might eventually lead to the formation of a surface α-Li_3BO_3 layer. A formation of α-Li_3BO_3 layer on the surface of Ni-rich cathode active materials has also been predicted by our simulation for B-doped $LiNiO_2$[20c] and $LiNi_{0.92}Co_{0.04}Al_{0.04}O_2$.[21] As can be seen in Figure 2b, despite a large displacement of B, O, and Li ions occurring during its formation, the curved like Li_3BO_3 structure is thermodynamically very stable (>5 eV per B) in comparison to the initial structure with B at the subsurface site. We believe that the Li_3BO_3 structure remains stable even after lattice delithiation as it forms only on the surface far from the Li sites in the bulk region.

The formation of a surface oxide layer takes place only for B-doped Ni-rich systems and not the Ru-doped ones. The segregation of Ru to the topmost surface layer is not energetically favorable, which might be due to the unfavorable lower coordination of TM sites for Ru at the surface compared to the bulk.

As B-doping leads to the formation of α-Li_3BO_3 surface coating, we compare the conductivity of NCM811 with that of Li_3BO_3. The ionic conductivity of α-Li_3BO_3 has been recently computed by Y. Li et al to be 3.2×10^{-7} S cm^{-1}, which is around two orders of magnitude higher than that for NCM cathodes (8.7×10^{-9} S cm^{-1} for NCM523 at 50 °C[23]).[24] For the case of Ru-doped NCM811 in which Ru prefers Ni site in bulk, we simulated Li-ion migration in the bulk model. The computed Li-ion diffusion barrier in pristine (0.60 eV) and Ru-doped (0.88 eV) cases (**Figure 3**) indicates that the ionic conductivity of the latter is lower. This is because of a large electrostatic repulsion between Li^+ and Ru^{4+} at the transition state. Moreover, we have calculated DOS for the (104) surface model to evaluate both bulk and surface contributions. Our calculations indicate the band gap of Ru-doped system is only slightly narrower, which might mean that the electronic conductivity of the Ru-doped NCM811 is slightly higher than in the pristine case. This result shows that the overall conductivity (ionic + electronic) of bulk NCM811 decreases by Ru doping. However, a significant lowering of conductivity is not expected as only a small amount of Ru dopant is found in the bulk lattice.

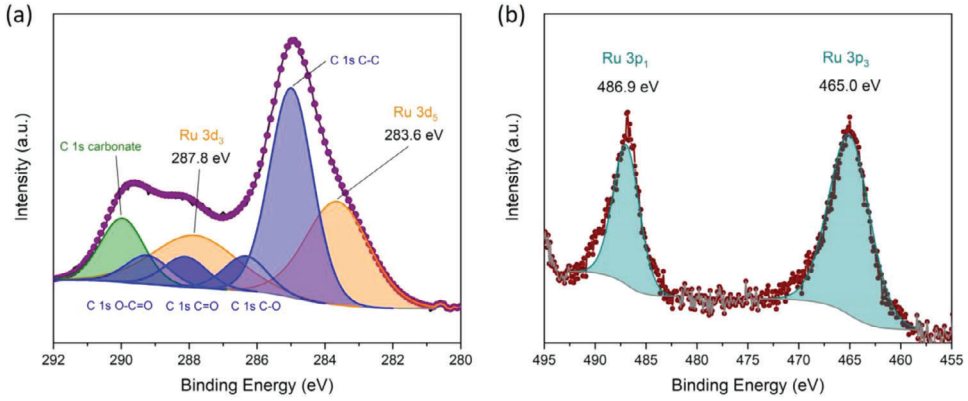

Figure 6. a) C 1s as well as Ru 3d and b) Ru 3p XPS spectra collected from 2Ru-NCM811.

Furthermore, we modeled a coherent twin grain boundary Σ31-12[110]/(112) for the Ru- and B-doped systems (**Figure 4**). We focused on the simple $LiNiO_2$ composition to reduce the complexity of the GB model. Geometry optimization with DFT-PBE+U leads to the sliding of grains along the GB resulting in the formation of an incoherent twin grain boundary. This is probably driven by the minimization of electrostatic interaction. The total energies of Ru- and B-doped NCM811-GB are listed in Table S1 (Supporting Information). It is found that Ru is energetically (by 40 meV per formula unit) more favorable at the incoherent GB site than in the bulk site. This result shows the tendency of Ru-doped NCM811 to form incoherent GBs resulting in the shrinkage of the primary particle size as well as lowering of Li-ion conductivity with Ru doping. The Ni cations at TM sites block the Li-ion pathway and can considerably decrease the conductivity of secondary particles. A similar trend has not been found for the B-doped case in which the occupation of a Ni site at GB by B is less favorable (190 meV per formula unit) compared to that in the bulk site (see Table S1, Supporting Information). As the absorption of B to the bulk is energetically less favorable than its surface segregation (Figure 2), we propose that B doping leads to the formation of lithium boron oxide on the surface of agglomerate and will not influence the size of primary particles.

2.2. Experiment

In experimental investigation, we extensively examined the microstructure, particle size, morphology, and electrochemical performances of 2 mol% Ru-doped NCM811 (2Ru-NCM811), while also making a comparative analysis with pristine NCM811 and 2 mol% B-doped NCM811 (2B-NCM811) as discussed in our previous studies.[7a] The chemical analysis by ICP-OES (Table S2, Supporting Information) confirms that the cathode materials have the targeted NCM composition and dopant (Ru and B) concentration. The powder XRD patterns of pristine, Ru-doped, and B-doped NCM811 indicate phase pure materials with a hexagonal α-$NaFeO_2$ structure, and the space group $R\bar{3}m$ (166) (**Figure 5**).[25]

The clear peak splitting of (006)/(102) at 38 – 38.5 °(2θ) and (108)/(110) at 64 – 65 °(2θ) (Figure 5b,c) indicates the presence of a well ordered hexagonal layered structure with high crystallinity.[26] No impurity phases were observed, and no additional reflections appeared by introducing the dopants. A slight peak shift toward smaller angles is observed. It is more pronounced for 2Ru-NCM811 and indicates a lattice expansion due to the incorporation of the dopant into the lattice (Figure 5b,c). These results agree with our DFT calculation (Table 1). For all cathode materials, a splitting of the Bragg reflections (108) and (110) is observed in Figure 5c. This peak splitting is device specific and caused by $k_{\alpha 2}$ radiation.

The lattice parameters for pristine, doped NCM811 were calculated from the XRD patterns using the Rietveld refinement (Table S3 and Figure S3, Supporting Information). The here obtained values for NCM811, fall within the span reported in literature ($a = 2.8661 - 2.8805$ Å; $c = 14.2021 - 14.249$ Å).[27] Compared to pristine NCM811, doping with 2 mol% Ru leads to a slight expansion of the lattice parameters a and c (Table 1), which was expected in view of peak shift observed in the XRD pattern and is consistent with the previous work on Ru-doped CAM.[19] Thus, the XRD analysis indicates that Ru was successfully incorporated into the NCM lattice. In the case of doping with the small-sized boron, the expansion of the lattice parameters is less significant. However, as reported previously, a successful incorporation of boron into the NCM lattice is possible, even if no lattice expansion is observed.[7a]

X-ray diffraction and Rietveld refinement results (Table S4, Supporting Information) indicate that B and Ru occupy the TM positions which was confirmed by DFT calculation as discussed above. A closer examination of the XRD patterns (Figure 5) in terms of the Bragg reflection intensity ratio $I(003)/I(104)$ and the splitting of the (108)/(110) Bragg reflections reveals additional effects of doping. By Ru and B doping, the $I(003)/I(104)$ ratio decreases (Table S3, Supporting Information) and the splitting of the (108)/(110) Bragg reflection is less intense in the Ru-doped sample. These observations are indicative of an enhanced cation disorder (Ni^{2+} occupies Li sites). The c/a ratio, which is an additional indicator of the degree of cation disorder shows decreased values for the doped cathode active materials. For an ideal hexagonal closed-packed lattice with $R\bar{3}m$ (166) and layered structure, $c/a = 4.99$. Partial cation mixing is indicated by $c/a < 4.96$. Thus, all cathode materials exhibit cation disorder, which is enhanced in 2B-NCM811 and 2Ru-NCM811 (Table S3, Supporting Information).

In comparison to boron with its fixed oxidation state of 3+, the oxidation state of Ru in Ru-doped NCM811 is not known. X-ray photoelectron spectroscopy (XPS) was used in order to determine the oxidation state of Ru by analyzing the binding energies. The Ni $2p_3$ region of the XPS spectrum (Figure S7, Supporting Information) indicates that the main oxidation state of nickel is 3+, since the obtained spectrum could be fitted with a set of peaks derived from NiOOH.[28] The XPS spectrum in **Figure 6a** shows that the Ru $3d_5$ and Ru $3d_3$ core peaks occur at 283.6 eV and 287.8 eV, respectively. The Ru $3d_5$ binding energy of 283.7 eV for Ru-doped NCM811 in this work, is in an agreement with that found by U. Manju et al.[30] for Ru^{5+} ions in $RuSr_2GdO_6$. The Ru 3d spectrum does not show an intense peak at 281.8 eV corresponding to $RuCl_3$[30] used as Ru source during the synthesis. This result indicates a successful incorporation of Ru into the NCM811 lattice accompanied by a change of the oxidation state of Ru to a higher value than 3+. Since the Ru 3d spectrum partially overlaps with the C 1s spectrum, the Ru 3p XPS spectrum (Figure 6b) was additionally analyzed. Fitting of the Ru 3p spectrum was not performed due to lack of literature data, but the binding energies for the Ru $3p_3$ and Ru $3p_1$ core peaks can be estimated from Figure 6b to be 465.0 and 486.9 eV, respectively. These binding energies are similar to those found by N. Voronina et al.[17c] for the Ru^{5+}—O binding energy in $Na[Ni_{2/3}Ru_{1/3}]O_2$, where the peaks were found at 465 and 487 eV, respectively. The comparison of the binding energies for Ru in 2Ru-NCM811 with the literature values of other material systems suggests that the oxidation state of Ru in our Ru-doped NCM811 is 5+. The measured oxidation state of Ru (5+) (Figure 6) agrees qualitatively with the computed one ($Ru^{+5-\Delta}$) for model II (Figure 1).

Furthermore, the effect of doping with dopants of different sizes and charges on the particle size and morphology were investigated. The analysis of the particle size distribution (PSD) shows that all powders consist of hard secondary particles with a D50 value of 13, 11, and 14 μm for the pristine NCM811,

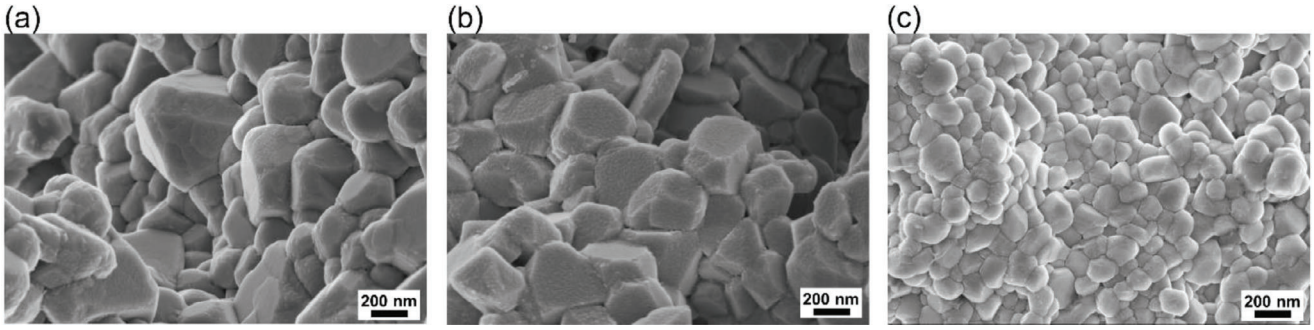

Figure 7. SE-SEM images (3 kV) showing primary particles of a) pristine NCM811, b) 2B-NCM811, and c) 2Ru-NCM811.

2Ru-NCM811, and 2B-NCM811, respectively (Figure S6, Supporting Information). Thus, the PSD of NCM811 is not strongly affected by doping. SEM analysis shows that the synthesized NCM811 powders consist of spherical agglomerates (Figure S5a–c, Supporting Information). Each individual agglomerate is composed of nano-sized cuboidal primary particles (**Figure 7**). The primary particles in pristine NCM811, Ru-doped NCM811, and B-doped NCM811 synthesized within this work by the same method (Figure S5d, Supporting Information) are randomly oriented and no alteration of the particle orientation by doping is achieved. However, Ru doping has a strong influence on the average primary particle size. While the primary particle size is around (318 ± 38) nm for pristine NCM811 (Figure 7a) and is not affected by B doping (297 ± 71) nm), it strongly decreases to (145 ± 38) nm for 2Ru-NCM811 (Figure 7c). Such reduced primary particle size agrees with the previous findings about Ru doping of different cathode materials.[18–19]

Smaller primary particles in the case of Ru doping were also predicted by our DFT calculation. As discussed before (Figure 4), Ru segregates to the grain boundaries. In general, it is known that dopants segregated to grain boundaries can change the relative grain boundary mobility and energy.[31] Thus, Ru doping possibly limits the grain growth during the calcination step, so that smaller primary particles form compared to pristine and B-doped NCM811, where a significantly stronger coarsening of the primary particles is observed. Moreover, the calculation emphasized that Ru can be incorporated into the NCM811 secondary particles while B enriches on the secondary particle surface.

To experimentally verify the theoretical findings, the pristine and doped NCM811 was analyzed by high-angle annular dark field scanning transmission electron microscopy (HAADF-STEM), energy-dispersive X-ray spectroscopy (EDS), ion beam analysis (IBA), and time-of-flight secondary ion mass spectrometry (ToF-SIMS).

The atomic resolved high angle annular dark field image (HAADF) in **Figure** 8a reveals the layered structure ($R\bar{3}m$) of pristine NCM811 up to the edge of the particle. The schematic structure of NCM811 fits to the visible layered structure, as the cation positions match the bright dotted rows in the Z-contrast image. In Figure 8b, the HAADF image of the B-doped NCM811 sample is presented. For more information on the different regions visible in this cutout of the original image, the reader is referred to ref. [7a] In short, two regions with a different structure were identified for the B-doped NCM. The FFT of the surface region (blue square) reveals the desired layered structure ($R\bar{3}m$), while in the bulk of the primary particle (green square) a rock-salt structure ($Fm\bar{3}m$) has formed. The Ru-doped samples are displayed in Figure 8c,d. In Figure 8c, the layered structure is visible and fits the corresponding 2Ru-NCM811 schematic structure. On the other hand, it is clearly visible that bright contrast spots at the edge of the particle can be found even on the Li positions. This could be due to Ni^{2+} occupying the Li sites. Such a cation disorder was found to be enhanced based on XRD and Rietveld refinement, especially for the doped samples (Table S3, Supporting Information). Taking into account that the DFT calculation suggests that the Ru is enriched at the grain boundaries, this could explain the appearance of atoms occupying the Li positions along the grain boundaries (Figure 8d). By taking a closer look at the upper edge of Figure 8d where such a grain boundary to a different oriented particle is shown, one can see that between the cation rows gradually an additional atom row becomes visible (yellow rectangle), this would support the suggestion. In order to further support the Ru segregation at such a grain boundary, electron energy loss spectroscopy (EELS) line scans were performed in the region shown in Figure 8d. However, due to the Ru-edge overlapping with the carbon background EELS was not able to define Ru in the sample. Therefore, the grain boundary and the adjacent primary particles shown in Figure 8d were further characterized by EDS (Figure 8e). The EDS mapping shows a homogenous distribution of all elements, including Ru dopant. This was confirmed for additional primary particles at a different position on the sample (Figure S8, Supporting Information), where the EDS spectrum shows the Ru-L_α and Ru-L_β peaks at 2.6 and 2.7 keV, respectively, in addition to the expected signals for Ni, Co, and Mn. The EDS analysis clearly confirms the presence of Ru in the primary particles, but a Ru enrichment at the grain boundary could not be proven by EDS since optimal sample properties such as stability under the electron beam would be required to provide an atomic resolution EDS mapping.

In addition to TEM and EDS, IBA and ToF-SIMS were used to experimentally verify the exact location of the dopants in NCM811. Rutherford backscattering spectrometry (RBS) was used to detect and quantify the Ru dopant. The RBS part of the spectrum of interest for Ru (Figure S9a, Supporting Information) shows a perfect match between the backscattering of Ru at around channel 780 and the simulated spectrum. The quantification of Ru based on RBS results in an average concentration of (2 ± 1) mol% Ru in the analyzed 2Ru-NCM811 powder in agreement with ICP-OES (Table S2, Supporting Information). Since the channel range of Ru in this measurement is very

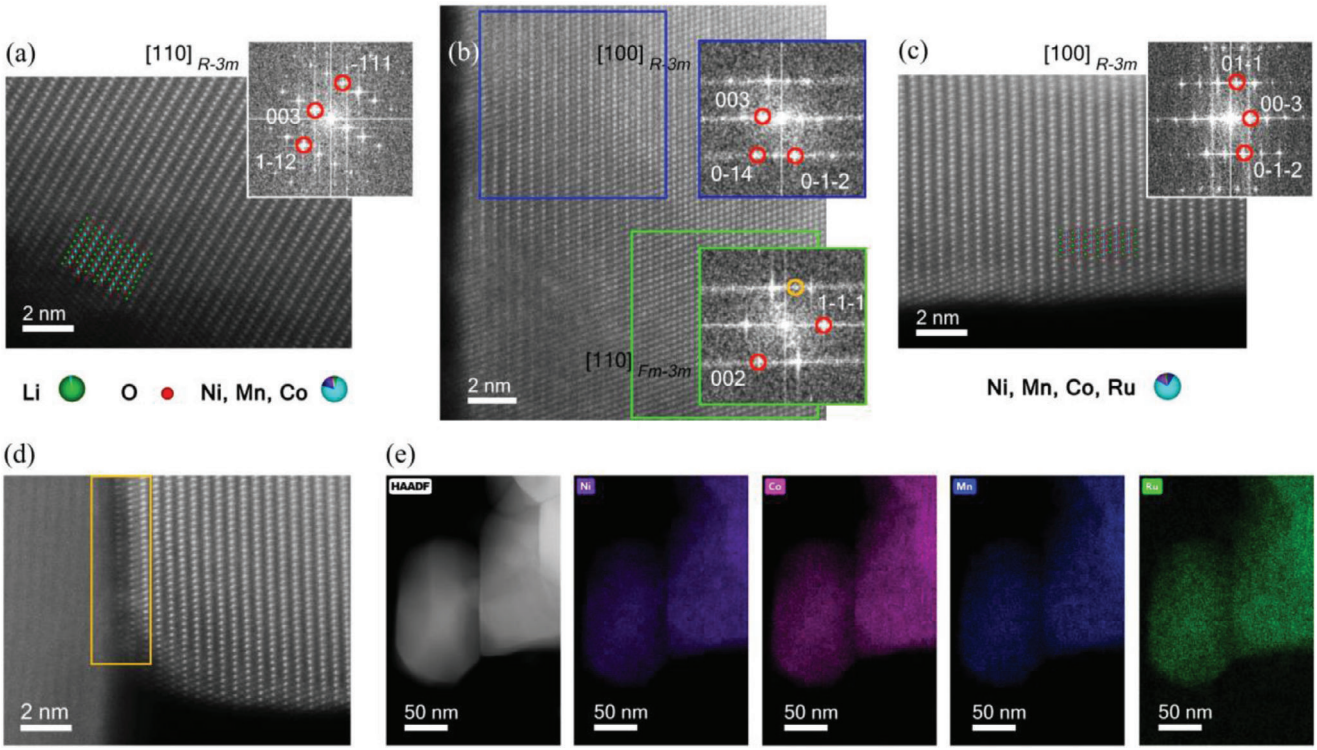

Figure 8. STEM images showing primary particles of a) pristine NCM811, b) 2B-NCM811, and c) 2Ru-NCM811 with their corresponding FFT´s. The FFT´s with white frames are taken out of the hole image while the blue and green framed FFT´s are taken out of the corresponding areas. d) Shows the grain boundary to a second 2Ru-NMC811 particle. e) HAADF-STEM image and EDS mappings for Ni, Co, Mn, and Ru of the grain boundary and the adjoining primary particles shown in d). Panels a) and b) are reprinted (adapted) with permission from ref. [7a]. Copyright 2022, American Chemical Society.

scarce, RBS provides only near-surface information. Therefore, particle induced X-ray emission (PIXE) was used since it enables a higher penetration depth. The PIXE spectrum (Figure S9b, Supporting Information) shows a clear, background free K_α and K_β signal at 19 and 21.5 keV, respectively. PIXE verifies the presence of Ru not only on the surface but also in the bulk of the Ru-doped NCM811 particles. In the case of 2B-NCM811, the light element boron was detected and quantified by nuclear reaction analysis (NRA), as presented in our previous work.[7a]

The surface of Ru- and B-doped NCM811 particles was further characterized by ToF-SIMS with positive polarity (**Figure 9**). Independent on the used dopant, the depth profiles show that the Ni^+, Co^+, and Mn^+ signals slightly increase and remain constant after a certain sputtering time. A possible reason for this finding is that the sputter ions remove surface contaminations (e.g., carbonates, hydroxides, etc.) formed during the transfer of the samples to the instrument. It is noted that the Ru^+ signal is nearly constant throughout the sputtering process (Figure 9a), indicating a constant Ru concentration on the surface of the secondary particles as well as in the bulk of the Ru-doped NCM811 primary particles. In the case of 2B-NCM811 (Figure 9b), the B^+ signal decreases with the sputtering time and stays constant after 150 s which indicates an enrichment of B on the secondary particle surface, as well as a significant high and constant concentration in the primary particles bulk, as discussed previously.[7a]

Furthermore, in contrast to B doping, which leads to a surface enrichment of boron on the secondary particles[7a] (Figure 9b), no gradient in the Ru-concentration was observed for 2Ru-NCM811. However, a homogenous concentration from the surface to the bulk was found. The results of TOF-SIMS analysis support the conclusions of XRD, EDS, and PIXE that the Ru is incorporated into the bulk structure of the core of the primary particles. As known from previous experimental and theoretical studies on NCA[22] and experimental work on NCM[20c] as well as our present theoretical work on NCM811 (Figure 2) boron atoms tend to segregate to the crystal surface.[20c] Such a phenomenon is not observed in the case of Ru doping.

Furthermore, the effects of doping on the NCM lattice with different-sized and charged dopants on the electrochemical properties of NCM811 were investigated. In the following, the electrochemical performance of Ru-doped NCM811 is compared to that of pristine NCM811 and 2B-NCM811 presented in our previous work.[7a] The CV curves of pristine NCM811, 2B-NCM811, and 2Ru-NCM811 (**Figure 10**a) confirm their electrochemical activity. As known for Ni-rich NCM811, also the doped NCM811 shows multiple redox peaks corresponding to the H1 to M, M to H2, and H2 to H3 phase transitions. However, the M to H2 and H2 to H3 transitions appear to be less pronounced for 2Ru-NCM811, as indicated by the lower peak currents compared to pristine NCM811 and 2B-NCM811. Although a $Ru^{4+} \leftrightarrow Ru^{5+}$ redox couple has already been reported for the spinel structure,[32] the hexagonal layered structure investigated here shows no any additional

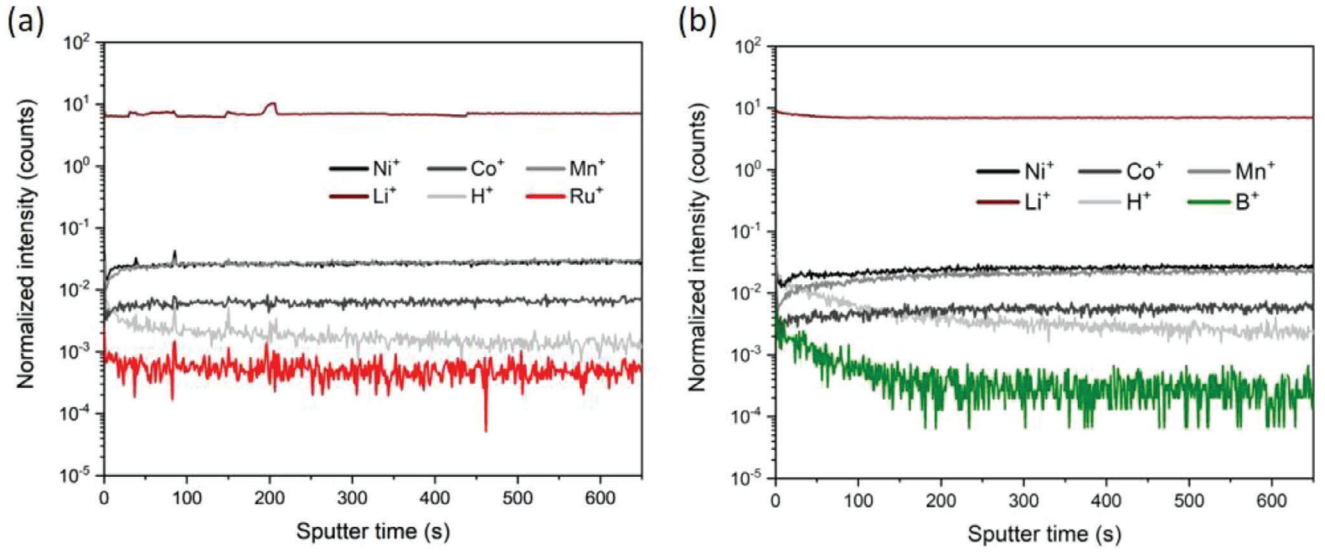

Figure 9. TOF-SIMS depth profiles of a) 2Ru-NCM811 and b) 2B-NCM811. The depth profile for 2B-NCM811 is reprinted (adapted) with permission from ref. [7a]. Copyright 2022, American Chemical Society.

peaks in the analyzed potential range. This either means that Ru is not electrochemically active in the selected potential window, the amount of Ru is too small to show a significant contribution in the CV curve, or that the redox peaks of Ru are superimposed by those of Ni and Co. The potential difference between the oxidation and reduction peaks at around 3.80 V is 0.11 V for pristine NCM811, 0.09 V for 2B-NCM811, and 0.14 V for 2Ru-NCM811. Thus, the Ru-doped NCM811 exhibits a larger potential difference, suggesting a higher polarization of the Ru-doped cathode due to slower insertion/extraction of Li ions in the layered structure. The increased polarization due to Ru doping is more evident in the first CV scan (Figure S10, Supporting Information).

The incorporation of Ru is evident also from the altered galvanostatic charge/discharge profiles (Figure 10b), which exhibit shorter and less intense charge/discharge plateaus at ≈4.2 V compared to the pristine NCM811 and 2B-NCM811. After an initial conditioning cycle, a discharge capacity of 191 and 193 mAh g^{-1} was obtained for pristine NCM811 and 2B-NCM811, respectively, while only 164 mAh g^{-1} was obtained for 2Ru-NCM811 (Figure 10b). The Coulombic efficiencies are 97 % for pristine NCM811, 98 % for 2B-NCM811 and 94 % for 2Ru-NCM811. Moreover, the rate performance test, prolonged cycling test at 0.5 C (Figure 10c) also show lower capacities for the Ru-doped sample compared to the undoped and B-doped cathode active material. By electrochemical impedance spectroscopy, a strongly enhanced contribution of the charge-transfer resistance in the medium to low-frequency range was found for 2Ru-NCM811 (Figure S12, Supporting Information). During long-term cycling, all samples show continuous capacity fading (Figure 10c). After 120 cycles, 88, 145, and 68 mAh g^{-1} were obtained for pristine NCM811, 2B-NCM811, and 2Ru-NCM811, respectively. The highest capacity retention was obtained for 2B-NCM811 (87 %) while the retention for 2Ru-NCM811 (62 %) is higher than that for pristine NCM811 (53 %). For all cathodes, similar Coulombic efficiencies were obtained during long-term cycling (Figure S11, Supporting Information).

Compared to previous studies about Ru-doped cathode active materials for LIBs,[18–19] 2 mol% Ru doping of NCM811 does not show the expected beneficial effects. Ru doping appears to have a detrimental effect on the electrochemical performance of NCM811. In general, a reduced capacity is a known side effect of doping as explained by M. Eilers-Rethwisch et al.[33] It should be noted that there is no evidence for the electrochemical activity of Ru in NCM811. If Ru is electrochemically inactive within the applied potential window, a decrease in gravimetric capacity is reasonable due to the high molar mass of Ru. The high oxidation state of Ru (Ru^{5+}), causes the formation of Li vacancies and increases the cation disorder, as verified by XRD (Table S3, Supporting Information), for charge balancing. Additionally, the introduction of Ru^{5+} ions into the transition metal sites can lead to the formation of more Ni^{2+} species which migrate to the Li layer resulting in an enhanced cation disorder. This applies also for other high valent dopants like W^{6+} as reported by G. Park et al.[34] A cation-disordered phase has a higher activation energy barrier for lithium diffusion, which is due to the smaller distance between the slabs and the barrier caused by the TM-ions in the lithium layer.[35] Moreover, our calculation (Figure 3) indicates a considerably higher diffusion barrier for Li-ion passing near $Ru^{+5-\Delta}$ (due to the strong $Ru^{+5-\Delta} - Li^{1+}$ repulsion) but only a slight decrease in the band gap in the Ru-doped case compared to the pristine one. This shows that the overall conductivity of bulk NCM811 decreases with Ru doping, but since only a small amount of Ru is found in the crystal the decrease is small. However, due to the significant increase in the diffusion barrier of Li ions that migrate close to a Ru dopant (see Figure 3a) as well as the structure of Ru-doped stabilized incoherent GB (see Figure 4a) in which the pathway of migrating Li ions from the Li plane of a grain to the nearby grain is blocked by its TM layer, the accumulation of Ru at the GBs can strongly slow the Li-ion diffusion. Therefore, a higher polarization and

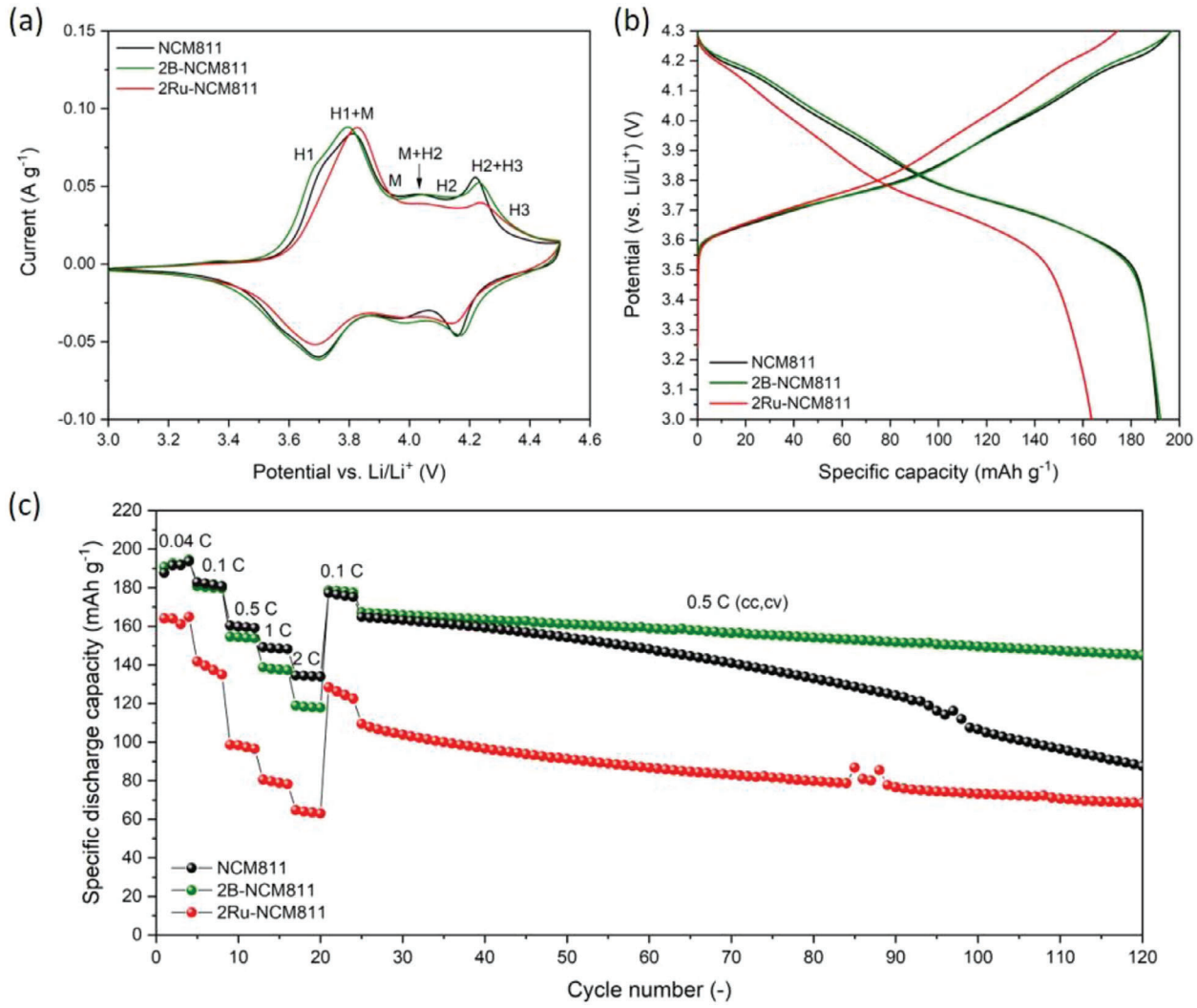

Figure 10. Electrochemical performance of NCM811, 2B-NCM811, and 2Ru-NCM811. a) Cyclic voltammogram curves at a scan rate of 0.05 mV s^{-1} for the second cycle. b) Galvanostatic charge–discharge profiles at 0.04 C for the second cycle. c) Rate capability tests at various C-rates with prolonged cycling at 0.5 C (cc, cv). The data for NCM811 and 2B-NCM811 are reprinted with permission from ref. [7a] Copyright 2022, American Chemical Society.

resistance can occur, and consequently, only a lower percentage of Li can de-/intercalate limiting the resulting charge/discharge capacities for Ru-doped NCM811. An overall lower Li utilization can explain the higher capacity retention after 120 cycles due to a reduced mechanical stress. It was found that Ru doping reduces the primary particle size, which leads to an enhanced number of grain boundaries that could negatively affect the cell resistance that was found to be strongly increased for 2Ru-NCM811.

In contrast to Ru doping, B doping improved the electrochemical performance of NCM811 during long-term cycling (Figure 10c).[7a] The main difference between these dopants is their effect on the surfaces and grain boundaries of NCM811. The Ru doping does not lead to the enrichment of the dopant on the secondary particle surface as it was reported for B doping. Due to surface enrichment of boron, the formation of a lithium boron oxide surface layer is suggested, which can serve as a protective coating and enable improved capacity retention during long-term cycling.

3. Conclusion

The impact of large size and charge of dopant ruthenium on the microstructural (summarized in **Figure 11**) and electrochemical properties of Ni-rich NCM811 was investigated and compared to that of dopant boron with small size and charge by a combined theoretical and experimental approach. It is found that ruthenium segregated to the gain boundaries and leads to a reduced primary particle size. Due to the large repulsion between Ru^{5+} and migrating Li^+ ions as well as the formation of incoherent grain boundaries that blocks Li^+ diffusion pathway, Li-ion conductivity in the case of Ru-doped is expected to be low, which can be one of the reasons for its low initial capacity at high C-rates. Furthermore, smaller primary particles expose more surfaces to the electrolyte which increases the side reaction between NCM811 surface and electrolyte. However, the small size and lower charged boron tends to enrich on the agglomerate surface forming a lithium boron oxide surface coating that protects the

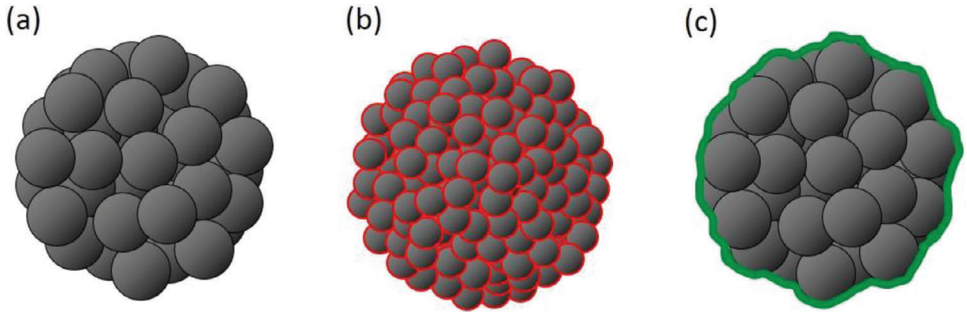

Figure 11. Schematic of a) pristine NCM811, b) 2Ru-NCM811, and c) 2B-NCM811 secondary particles showing the distribution of dopants (red: Ru, green: B) and their impacts on the morphology.

NCM811 surface from aggressive electrolyte attacking. Thus, B-doped NCM811 shows superior electrochemical performances than the pristine and Ru-doped materials. In this work, we indicate that the effect of doping on bulk properties such as lattice parameters and charge states of ions is very small. However, it shows a significant effect on gain boundaries between the primary particles of Ni-rich layered oxide materials and their exposed surfaces to the electrolyte, which correlates to the dopant size and charge state.

4. Experimental Section

Theoretical Section: *Bulk*: Total Coulomb energy (E_c) analysis and density functional theory (DFT) calculations were used to find the most favorable atomistic structures of Ru-doped NCM811.[36] E_c calculations on various possible combinations were carried out using the *supercell* code.[37] Spin-polarized DFT calculations were performed with the Projector Augmented-Wave (PAW)[38] pseudopotential method implemented in the Vienna Ab initio Simulation Package (VASP) code.[39] The Perdew–Burke–Ernzerhof (PBE) functional of generalized gradient approximation (GGA)[40] was applied for determining the atomistic structures. To estimate the lattice parameter changes with delithiation, the PBE functional with Hubbard U and dispersion correction (i.e., PBE + U and DFT + D3) are included for DFT calculations. The Hubbard U parameters U–J = 6.0, 5.9, 5.2, and 8.0 eV were used for Ni, Co, Mn, and Ru, respectively. Moreover, the DFT with Heyd–Scuseria–Ernzerhof (HSE) functional[42] was used to calculate the electronic structures. The $Li[Ni_{0.8}Co_{0.1}Mn_{0.1}]O_2$ (NCM811) bulk was modeled using a 4 × 4 × 1 ($Li_{48}Ni_{40}Co_4Mn_4O_{96}$) supercell.[3] Two models were considered for Ru-doped NCM811 to find the atomistic structures of Ru-doped NCM811. For model I, all possible configurations for 1 Ru in 36 Ni sites with four fixed Ni were modeled. These four Ni were determined from the previous study which shows the charge state of 2+.[3] Moreover, we considered one extra Ni^{2+} in 36 Ni sites to balance the charge. Thus, we have $\frac{36!}{1!35!} \times \frac{35!}{1!34!} = 1260$ configurations ($Li_{48}Ni_{39}Co_4Mn_4Ru_1O_{96}$) in total. The most favorable structure was found to be the one with Ru in between Mn in Ni/Mn layer after E_c calculations. To compare the total free energies with DFT-PBE, we also modeled Ru at Ni/Ni and Ni/Co layers. Finally, the most favorable structure of Ru doped in NCM811 was found in the Ni/Mn layer. For model II, the Ru-doped NCM811 with 1 Li vacancy was investigated. For E_c calculation, we modeled all possible arrangements of removing 1 Li from 48 Li sites and replacing 1 Ru in 36 Ni sites with 4 fixed Ni, namely $\frac{48!}{1!47!} \times \frac{36!}{1!35!} = 1728$ configurations ($Li_{47}Ni_{39}Co_4Mn_4Ru_1O_{96}$). The Ru replaced Ni site in Ni/Mn layer with the Li vacancy nearby was the most favorable structure for E_c calculations. To find the most favorable configuration, the structures with Ru in Ni/Ni and Ni/Co layers were also modeled and their total energies were computed by DFT-PBE. Finally, the most favorable structure was found to be the one with Ru at the Ni/Ni layer with 1 Li vacancy. The charge value of Ni was 2+ and 3+, while Co is 3+ and Mn is 4+ for all above E_c calculations. For Li and O, we applied the charge value of 1+ and 2− , respectively. A 2 × 2 × 1 k-point mesh and an energy cutoff of 500 eV as well as an energy and force convergence criterion of 10^{-4} eV and 10^{-3} eVÅ^{-1}, respectively, were used for DFT-PBE and PBE + U calculations on atomistic structures. The spin density difference (SDD) and number of unpaired electrons (NUE) and density of state (DOS) were simulated by a 1 × 1 × 1 k-point mesh with electronic and force convergence criterion of 10^{-6} eV and 10^{-5} eVÅ^{-1}, respectively, for DFT-HSE calculations. The atomistic structures and SDD were visualized with the VESTA program.[43] The energy barriers (E_b) for Li-ion diffusion were computed using the DFT-nudged elastic band (NEB) calculation. We considered five images for DFT-NEB calculations. *Surface*: To calculate surface segregation and energies of bare, Ru- and B-doped NCM811, (003) and (104) surfaces were modeled. The B-doped Li-rich nonstoichiometric $LiNiO_2$ (003) surface with and without boron oxides in the recent work[20c] were used to model structures of Ru- and B-doped NCM811 on (003) surfaces. The (003) surfaces were calculated by a vacuum space of 28 Å. The (104) surface of Ru-doped NCM811 was constructed from the model II. The Ni sites on the surface and in the subsurface were studied to find the favorable site of Ru and B. Five-layer slabs for (104) surfaces were used and a vacuum space of at least 12 Å between slabs was introduced. A 1 × 5 × 1 and a 1 × 2 × 1 k-point mesh was applied for simulating (003) and (104) surface, respectively. An energy cutoff of 600 eV as well as an energy and force convergence criterion of 10^{-4} eV and 10^{-3} eV Å^{-1} were used for DFT-PBE calculations. Grain Boundary: The DFT-PBE calculation was performed to compute the atomistic structures of twin grain boundaries. A 2 × 2 × 1 k-point mesh and an energy cutoff of 600 eV as well as an energy and force convergence criterion of 10^{-4} eV and 10^{-3} eV Å^{-1}, respectively, were used for DFT-PBE calculations. The atomistic structures and SDD were visualized with the VESTA program.[43]

Cathode Material Synthesis: Pristine $LiNi_{0.8}Co_{0.1}Mn_{0.1}O_2$ (NCM811) and 2 mol% B-doped $LiNi_{0.8}Co_{0.1}Mn_{0.1}O_2$ (2B-Li1.0NCM811) were synthesized by a hydroxide co-precipitation route reported before.[7a] For the synthesis of the 2 mol% Ru-doped NCM811 precursor, $RuCl_3 \cdot xH_2O$ (Alfa Aesar, 99.9 %) was dissolved in deionized water and a desired volume of the resulting solution, with a Ru content of 39.8 g L^{-1}, was added to the transition metal solution to realize a molar ratio of Ru:(Ni + Co + Mn) = 0.023:1. Afterward, the co-precipitation of the Ru-doped hydroxide precursor was performed in exactly the same way as reported for the pristine NCM811 precursor. In order to form the final, 2 mol% Ru-doped $LiNi_{0.8}Co_{0.1}Mn_{0.1}O_2$ (2Ru-NCM811), the hydroxide precursors were mixed with LiOH (Merck, 98 %) in a molar ratio of Li:(Ni + Co + Mn) = 1.03:1. The mixture was thoroughly ground in an agate mortar and calcined in an Al_2O_3 crucible for 5 h at 480 °C, and subsequently for 10 h at 800 °C under a pure O_2 atmosphere, whereas heating and cooling rates of 5 K min^{-1} were applied.

Material Characterization: The chemical composition of the NCM powders was analyzed by inductively coupled plasma-optical emission

spectrometry (ICP-OES) by using a Thermo Scientific iCAP7600 (Thermo Fischer Scientific, USA). The particle size distribution (PSD) was measured by a laser diffraction particle size distribution analyzer (La-950, Horiba Ltd., Japan). The evaluation was based on the Mie-theory by using a refractive index of 1.24 for NCM.[44] The synthesized NCM powders were characterized for phase purity and crystal structure by using X-ray diffraction (XRD). X-ray powder diffraction was carried out using a D4 ENDEAVOR (Bruker Corporation, USA) with Cu-K_α radiation. For the qualitative phase analysis, powder XRD data were collected in a 2θ range of 10 – 80 °, with a step of 0.02 ° and a collecting time of 0.75 s/step. In the case of measurements for Rietveld refinement, a 2θ range of 10 – 140 ° was chosen. The qualitative phase analysis of the diffraction patterns was carried out based on the powder diffraction file (PDF) database and the inorganic crystal structure database (ICSD) using the software HighScore (Malvern Panalytical Ltd, UK).[44] Crystal structural refinement and determination of lattice parameters by means of Rietveld refinements were carried out using the program FullProf.[45] For morphology investigations and phase determination, scanning electron microscope (SEM) images were taken by using a Zeiss Gemini 450 (Carl Zeiss Microscopy Deutschland GmbH, Germany). The powders were prepared on sticky carbon tape and coated with a thin platinum layer. Secondary particle cross-sections were prepared by focused ion beam (FIB) with a 15 nA (initial) and 700 pA (final) Ga beam and analyzed using a Zeiss Crossbeam 540 SEM (Carl Zeiss Microscopy Deutschland GmbH, Germany). An aberration-corrected FEI Titan G2 80–200 ChemieSTEM field emission electron microscope at 200 kV was used for high-angle annular dark field (HAADF) imaging and acquisition of energy-dispersive X-ray (EDS) elemental mapping. The FEI Titan G2 80–200 ChemiSTEM is equipped with a Schottky-type high-brightness electron gun (FEI X-FEG), a Cs probe corrector (CEOS DCOR), an in-column Super-X energy dispersive X-ray spectroscopy unit (ChemiSTEM technology), a post-column energy filter system (Gatan Enfinium ER 977) with dual electron energy-loss spectroscopy (EELS) option allowing a simultaneous read-out of EDX and EELS signals at a speed of 1000 spectra per second.[46] The powder samples were prepared just before the microscopy session by drop casting the sample on a 200 Mesh copper carbon film grid. For X-ray photoelectron spectroscopy (XPS), a 200 µm spot of the powder sample, prepared on an indium foil, was analyzed by using a Phi5000 VersaProbe II (ULVAC-Phi Inc., USA) spectrometer with monochromatic Al K_α radiation (1.486 keV). For the analysis, 23.5 eV pass energy, 0.1 eV steps, and 100 ms/step were applied. The charge correction was performed by setting the C—C component of the C 1s signal to 285 eV. The characterization of the Ru-doped NCM811 powder by ion beam analysis (IBA) was carried out in a sample holder specially developed for the analysis of powders by IBA. This powder sample holder was made of aluminum and equipped with a 500 nm thick SiN window that was optically transparent for the beams. Ruthenium was detected by RBS and PIXE using 2960 keV protons and Si-detectors for simultaneous detection of the RBS and PIXE spectra. The evaluation of the IBA data was performed with the SimNRA 7.02 software.[47] Time of flight secondary-ion mass spectrometry (TOF-SIMS) was applied for depth profiling using a TOFSIMS_5.NCS system (ION-TOF GmbH, Germany). The powders were prepared by spreading them on an indium foil and fixing them through self-adhesion. A 30 keV Bi^+ primary beam for analysis and a 1 keV O_2^+ beam for sputtering (to alter the analysis depth of the measurement) was scanned over an area of 400 µm × 400 µm, operating under a non-interlaced mode and using a 1 s:1 s sputter:analyze cycle. The analyzed area by the Bi beam was 130 µm × 130 µm, with either positive or negative secondary ions detected. Data analysis was carried out with the SurfaceLab 7.0 (ION-TOF GmbH, Germany) software. The intensities were normalized to $^6Li^+$.

Electrochemical Characterization: In order to investigate the electrochemical activity, electrodes with an active material loading of ≈5 mg cm^{-2} were fabricated by casting a cathode slurry onto an Al foil current collector. The slurries were prepared by mixing NCM, carbon black (Alfa Aesar, Super P Conductive, 99+ % metal basis), and poly(vinylidene fluoride) (PVDF) (Alfa Aesar, mp:155 – 160 °C) with a weight ratio of 90:5:5 in N-methyl-2-pyrolidone (NMP) (Alfa Aesar, 99+ %). A gap-bar coater (MSK-AFA-HC100, MTI Corporation, USA) with vacuum and heating function was used to cast the slurry on an Al foil. The resulting tape was afterward dried at 120 °C and further dried in a vacuum furnace (VO 500, Memmert GmbH + Co.KG, Germany) at 80 °C for 12 h. Coin cells (CR2032) were assembled in an argon filled glovebox by using the NCM cathodes, a glass fiber separator (Whatman), and a Li metal foil (Alfa Aesar) as anode. As electrolyte a 1.0 M solution of $LiPF_6$ (Sigma–Aldrich, battery grade) dissolved in an ethylene carbonate (Sigma–Aldrich, 99 %)/dimethyl carbonate (Sigma–Aldrich, 99 %)/ethylmethyl carbonate (Sigma–Aldrich, 99 %) mixture (1:1:1 by volume) with 2 wt.% vinylene carbonate (Sigma–Aldrich, 99.5 %) additive was used. The electrochemical tests were carried out by using a multipotentiostat (VMP-300, BioLogic Sciences Instruments, France) combined with a climate chamber (VT 4002EMC, Vötsch Industrietechnik GmbH, Germany) at a constant temperature of 25 °C. Cyclic voltammetry (CV) was performed in a potential range from 3.0 – 4.5 V versus Li/Li^+ with a scan rate of 0.05 mV s^{-1}. Galvanostatic cycling was performed at different C-rates (0.04, 0.1, 0.5, 1, and 2 C; 1C = 160 mA g^{-1}) in a voltage range of 3.0 – 4.3 V versus Li/Li^+. After the rate capability test long-term cycling was performed by constant current (cc) charge discharge at 0.5 C followed by constant voltage (cv) charge–discharge until a current of C/10 was reached. Electrochemical impedance spectroscopy (EIS) was performed at 4.3 V in a frequency range from 1 MHz to 10 mHz with an amplitude of 10 mV.

The data were evaluated by the software EC-lab (BioLogic Sciences Instruments, France).

Supporting Information

Supporting Information is available from the Wiley Online Library or from the author.

Acknowledgements

L.-Y.K. and C.R. contributed equally to this work. The financial support of this work by the German Federal Ministry of Education and Research (Bundesministerium für Bildung und Forschung, BMBF), within the projects "SimCaMat" (Grant No. 3EK3054A), "FestBatt2-Oxide" (FKZ: 13XP0434A) and "MeetHiEnD III" (FKZ: 13XP0258B, 03XP0258C), is acknowledged. The authors acknowledge the contributions of, Volker Nischwitz (ICP-OES), Heinrich Hartmann (XPS), Doris Sebold (SEM), Beatrix Göths (FIB-SEM), Sahir Naqash (ToF-SIMS), Markus Mann (Rietveld refinements), Andrea Hilgers (PSD), Volker Bader (heat treatments), and Philipp Hecker (heat treatments and lab assistance). L.-Y. Kuo acknowledges the Ministry of Science and Technology, Taiwan for their support through Project No: MOST 111-2222-E-131-002. P. K. and L.-Y. Kuo acknowledge the computing time granted through JARA-HPC on the supercomputer JURECA at Forschungszentrum Jülich.

Open access funding enabled and organized by Projekt DEAL.

Conflict of Interest

The authors declare no conflict of interest.

Data Availability Statement

The data that support the findings of this study are available from the corresponding author upon reasonable request.

Keywords

density functional theory, doping, Ni-rich cathode material, structural stability

Received: September 8, 2023
Revised: December 21, 2023
Published online:

[1] a) H.-H. Ryu, H. H. Sun, S.-T. Myung, C. S. Yoon, Y.-K. Sun, *Energy Environ. Sci.* **2021**, *14*, 844; b) W. Liu, P. Oh, X. Liu, M. J. Lee, W. Cho, S. Chae, Y. Kim, J. Cho, *Angew. Chem., Int. Ed. Engl.* **2015**, *54*, 4440; c) V. Etacheri, R. Marom, R. Elazari, G. Salitra, D. Aurbach, *Energy Environ. Sci.* **2011**, *4*, 3243.

[2] a) A. Chakraborty, S. Kunnikuruvan, S. Kumar, B. Markovsky, D. Aurbach, M. Dixit, D. T. Major, *Chem. Mater.* **2020**, *32*, 915; b) Z. Li, B. Zhang, G. Li, S. Cao, C. Guo, H. Li, R. Wang, J. Chen, L. Wu, J. Huang, Y. Bai, X. Wang, *J. Energy Chem.* **2023**, *84*, 11; c) Z. Li, H. Li, S. Cao, W. Guo, J. Liu, J. Chen, C. Guo, G. Chen, B. Chang, Y. Bai, X. Wang, *Chem. Eng. J.* **2023**, *452*, 139041.

[3] L.-Y. Kuo, O. Guillon, P. Kaghazchi, *ACS Sustainable Chem. Eng.* **2021**, *9*, 7437.

[4] a) N. Y. Park, H. H. Ryu, L. Y. Kuo, P. Kaghazchi, C. S. Yoon, Y. K. Sun, *ACS Energy Lett.* **2021**, *6*, 4195; b) H.-J. Noh, S. Youn, C. S. Yoon, Y.-K. Sun, *J. Power Sources* **2013**, *233*, 121.

[5] R. Dang, Y. Qu, Z. Ma, L. Yu, L. Duan, W. Lü, *J. Phys. Chem. C* **2022**, *126*, 151.

[6] A. Liu, N. Zhang, H. Li, J. Inglis, Y. Wang, S. Yin, H. Wu, J. R. Dahn, *J. Electrochem. Soc.* **2019**, *166*, A4025.

[7] a) C. Roitzheim, L.-Y. Kuo, Y. J. Sohn, M. Finsterbusch, S. Möller, D. Sebold, H. Valencia, M. Meledina, J. Mayer, U. Breuer, P. Kaghazchi, O. Guillon, D. Fattakhova-Rohlfing, *ACS Appl. Energy Mater.* **2022**, *5*, 524; b) Y.-J. Guo, C.-H. Zhang, S. Xin, J.-L. Shi, W.-P. Wang, M. Fan, Y.-X. Chang, W.-H. He, E. Wang, Y.-G. Zou, X. a. Yang, F. Meng, Y.-Y. Zhang, Z.-Q. Lei, Y.-X. Yin, Y.-G. Guo, *Angew. Chem., Int. Ed.* **2022**, *61*, e202116865.

[8] U. H. Kim, L. Y. Kuo, P. Kaghazchi, C. S. Yoon, Y. K. Sun, *ACS Energy Lett.* **2019**, *4*, 576.

[9] Z. Liu, J. Li, M. Zhu, L. Wang, Y. Kang, Z. Dang, J. Yan, X. He, *Materials* **2021**, *14*, 1816.

[10] S. Jeong, S. Park, M. Beak, J. Park, J. S. Sohn, K. Kwon, *Materials* **2021**, *14*, 2464.

[11] S. Gao, X. Zhan, Y.-T. Cheng, *J. Power Sources* **2019**, *410–411*, 45.

[12] N. Kiziltas-Yavuz, A. Bhaskar, D. Dixon, M. Yavuz, K. Nikolowski, L. Lu, R.-A. Eichel, H. Ehrenberg, *J. Power Sources* **2014**, *267*, 533.

[13] C. Sun, W. Chen, P. Gao, H. Hu, J. Zheng, Y. Zhu, *Ionics* **2022**, *28*, 747.

[14] B. Chu, L. You, G. Li, T. Huang, A. Yu, *ACS Appl. Mater. Interfaces* **2021**, *13*, 7308.

[15] a) F. A. Susai, D. Kovacheva, T. Kravchuk, Y. Kauffmann, S. Maiti, A. Chakraborty, S. Kunnikuruvan, M. Talianker, H. Sclar, Y. Fleger, B. Markovsky, D. Aurbach, *Materials* **2021**, *14*, 2070; b) H. H. Sun, U.-H. Kim, J.-H. Park, S.-W. Park, D.-H. Seo, A. Heller, C. B. Mullins, C. S. Yoon, Y.-K. Sun, *Nat. Commun.* **2021**, *12*, 6552.

[16] R. Shannon, *Acta Crystallogr. A* **1976**, *32*, 751.

[17] a) M. Sathiya, G. Rousse, K. Ramesha, C. P. Laisa, H. Vezin, M. T. Sougrati, M. L. Doublet, D. Foix, D. Gonbeau, W. Walker, A. S. Prakash, M. Ben Hassine, L. Dupont, J. M. Tarascon, *Nat. Mater.* **2013**, *12*, 827; b) M. Sathiya, A. M. Abakumov, D. Foix, G. Rousse, K. Ramesha, M. Saubanère, M. L. Doublet, H. Vezin, C. P. Laisa, A. S. Prakash, D. Gonbeau, G. VanTendeloo, J. M. Tarascon, *Nat. Mater.* **2015**, *14*, 230; c) N. Voronina, N. Yaqoob, H. J. Kim, K.-S. Lee, H.-D. Lim, H.-G. Jung, O. Guillon, P. Kaghazchi, S.-T. Myung, *Adv. Energy Mater.* **2021**, *11*, 2100901.

[18] H. Wang, T. A. Tan, P. Yang, M. O. Lai, L. Lu, *J. Phys. Chem. C* **2011**, *115*, 6102.

[19] B. Song, M. O. Lai, L. Lu, *Electrochim. Acta* **2012**, *80*, 187.

[20] a) C.-H. Jung, D.-H. Kim, D. Eum, K.-H. Kim, J. Choi, J. Lee, H.-H. Kim, K. Kang, S.-H. Hong, *Adv. Funct. Mater.* **2021**, *31*, 2010095; b) S.-H. Lee, B.-S. Jin, H.-S. Kim, *Sci. Rep.* **2019**, *9*, 17541; c) K.-J. Park, H.-G. Jung, L.-Y. Kuo, P. Kaghazchi, C. S. Yoon, Y.-K. Sun, *Adv. Energy Mater.* **2018**, *8*, 1801202.

[21] H.-H. Ryu, N.-Y. Park, J. H. Seo, Y.-S. Yu, M. Sharma, R. Mücke, P. Kaghazchi, C. S. Yoon, Y.-K. Sun, *Mater. Today* **2020**, *36*, 73.

[22] F. Stewner, *Acta Crystallogr. B* **1971**, *27*, 904.

[23] R. Amin, Y.-M. Chiang, *J. Electrochem. Soc.* **2016**, *163*, A1512.

[24] Y. Li, Z. D. Hood, N. A. W. Holzwarth, *Phys. Rev. Mater.* **2021**, *5*, 85402.

[25] C.-C. Chang, P. N. Kumta, *Mater. Sci. Eng., B* **2005**, *116*, 341.

[26] J. Zhu, T. Vo, D. Li, R. Lu, N. M. Kinsinger, L. Xiong, Y. Yan, D. Kisailus, *Cryst. Growth Des.* **2012**, *12*, 1118.

[27] a) A. O. Kondrakov, H. Geßwein, K. Galdina, L. de Biasi, V. Meded, E. O. Filatova, G. Schumacher, W. Wenzel, P. Hartmann, T. Brezesinski, J. Janek, *J. Phys. Chem. C* **2017**, *121*, 24381; b) F. Friedrich, B. Strehle, A. T. S. Freiberg, K. Kleiner, S. J. Day, C. Erk, M. Piana, H. A. Gasteiger, *J. Electrochem. Soc.* **2019**, *166*, A3760; c) X. Zheng, X. Li, B. Zhang, Z. Wang, H. Guo, Z. Huang, G. Yan, D. Wang, Y. Xu, *Ceram. Int.* **2016**, *42*, 644; d) S. Gao, Y.-T. Cheng, M. Shirpour, *ACS Appl. Mater. Interfaces* **2019**, *11*, 982.

[28] M. C. Biesinger, B. P. Payne, A. P. Grosvenor, L. W. M. Lau, A. R. Gerson, R. S. C. Smart, *Appl. Surf. Sci.* **2011**, *257*, 2717.

[29] U. Manju, V. P. S. Awana, H. Kishan, D. D. Sarma, *Phys. Rev. B* **2006**, *74*, 245106.

[30] J. F. Moulder, W. F. Stickle, P. E. Sobol, K. D. Bomben, *Handbook of X-ray Photoelectron Spectroscopy*, Perkin-Elmer Corp, Eden Prairie, MN **1992**.

[31] M. N. Rahaman, in *Ceramic Processing and Sintering*, CRC Press, Boca Raton, Florida **2003**.

[32] M. Reddy, S. S. Manoharan, J. John, B. Singh, G. S. Rao, B. Chowdari, *J. Electrochem. Soc.* **2009**, *156*, A652.

[33] M. Eilers-Rethwisch, M. Winter, F. M. Schappacher, *J. Power Sources* **2018**, *387*, 101.

[34] G.-T. Park, H.-H. Ryu, N.-Y. Park, C. S. Yoon, Y.-K. Sun, *J. Power Sources* **2019**, *442*, 227242.

[35] W. Liu, P. Oh, X. Liu, M.-J. Lee, W. Cho, S. Chae, Y. Kim, J. Cho, *Angew. Chem., Int. Ed.* **2015**, *54*, 4440.

[36] L. Y. Kuo, O. Guillon, P. Kaghazchi, *J. Mater. Chem. A* **2020**, *8*, 13832.

[37] K. Okhotnikov, T. Charpentier, S. Cadars, *J. Cheminf.* **2016**, *8*, 17.

[38] P. E. Blöchl, *Phys. Rev. B* **1994**, *50*, 17953.

[39] G. Kresse, J. Furthmüller, *Phys. Rev. B* **1996**, *54*, 11169.

[40] J. P. Perdew, K. Burke, M. Ernzerhof, *Phys. Rev. Lett.* **1996**, *77*, 3865.

[41] J. Heyd, G. E. Scuseria, M. Ernzerhof, *J. Chem. Phys.* **2003**, *118*, 8207.

[42] K. Momma, F. Izumi, *J. Appl. Crystallogr.* **2011**, *44*, 1272.

[43] K. Shizuka, K. Okahara, Layered lithium nickel manganese cobalt composite oxide powder for material of positive electrode of lithium secondary battery, process for producing the same, positive electrode of lithium secondary battery therefrom, and lithium secondary battery. U.S. Patent No. 8,354,191. 15 January, **2013**.

[44] T. Degen, M. Sadki, E. Bron, U. König, G. Nénert, *Powder Diffr.* **2014**, *29*, S13.

[45] J. Rodríguez-Carvajal, *Phys. B* **1993**, *192*, 55.

[46] A. Kovács, R. Schierholz, K. Tillmann, *J. Large-Scale Res. Facilities JLSRF* **2016**, *2*, 43.

[47] M. Mayer, *SIMNRA User's Guide*, Max-Planck-Institut für Plasmaphysik Garching, **1997**.